About the ellipticity of the discrete Laplacian in polar coordinate with Neumann condition

Benoît Trouette, Claudine Delcarte, Gérard Labrosse

About the ellipticity of the discrete Laplacian in polar coordinate with Neumann condition

B. Trouette[a,*], C. Delcarte[a], G. Labrosse[a]

[a] *Université Paris Sud 11, LIMSI-CNRS, B.P. 133, 91403 Orsay Cedex, France*

Abstract

The Chebyshev Gauss-Radau discrete version of the polar-diffusion operator, $\left(\frac{1}{r}\frac{\partial}{\partial r}\left(r\frac{\partial}{\partial r}\right)-\frac{k^2}{r^2}\right)$, k being the azimuthal wave number, presents complex conjugate eigenvalues when it is associated with Neumann boundary condition imposed at $r=1$. It is shown that this ellipticity violation of the original continuous problem is genuine and not due to some round-off error. A way to avoid these complex conjugate eigenvalues is proposed, at the expense of some loss of accuracy. An evaluation is performed of the impact this approach has on the spectral accuracy of the solution.

Keywords: polar laplacian, spectral collocation method, ellipticity, mapping

1. Introduction

Temporal discretization of the balance equations which govern the flow dynamics often leads to elliptic Helmholtz equations. When these multidimensional elliptic problems are separable, and posed in orthogonal geometries, their numerical solution can be efficiently obtained by using the Successive Diagonalization Technique (SDT), ([1, 2]). This method amounts to work in the Helmholtz operator numerical eigenspace, itself being tensiorally constructed from the eigenspaces of the second derivatives (see [1]). Making use of a spectral collocation method leads then to cheap accurate numerical solutions of a large variety of diffusion problems, with any kind of boundary conditions, Dirichlet, Neumann or Robin,

*Corresponding author

Email addresses: benoit.trouette@limsi.fr (B. Trouette), claudine.dang-vu-delcarte@limsi.u-psud.fr (C. Delcarte), gerard.labrosse@u-psud.fr (G. Labrosse)

with constant coefficients. This approach has been extended in [3] to the case where the boundary conditions involve mixed tangential and normal derivatives.

The key-point which makes this SDT attractive, for easy to implement, is the ellipticity of the original continuous problem, provided this ellipticity be preserved at the discrete step. This occurs in most of the cases, for instance in the Cartesian configuration, viz. with $\frac{\partial^2}{\partial z^2}$ completed with any boundary condition imposed at $z = \pm 1$. In cylindrical coordinates, the easy implementing of the SDT depends therefore upon the ellipticity of the companion operator of $\frac{\partial^2}{\partial z^2}$, namely the polar operator $\left(\frac{1}{r}\frac{\partial}{\partial r}\left(r\frac{\partial}{\partial r}\right) - \frac{k^2}{r^2}\right)$, k being the azimuthal wave number. The polar ellipticity is preserved in its Chebyshev Gauss-Radau discrete version when a Dirichlet boundary condition is imposed at $r = 1$, say. When a Neumann condition is imposed at $r = 1$, a few couples of complex conjugated eigenvalues show up for given values of k when the radial cut-off frequency N gets larger than 12. This paper will show that the presence of these complex eigenvalues, which violates the ellipticity of the original polar problem, is genuine and not due to some round-off error amplification associated itself with the bad conditioning of the Gauss-Radau matrix. A way to avoid these complex conjugated eigenvalues, in implementing the SDT, is proposed, at the expense of some loss of accuracy. An evaluation is made of the impact this approach has on the spectral accuracy of the solution.

2. Continuous problems

2.1. The inhomogeneous problem

Let us consider the diffusion equation in polar coordinates ($\mathbf{e_r}$,$\mathbf{e}_\phi$),

$$\left(\frac{1}{r}\frac{\partial}{\partial r}\left(r\frac{\partial}{\partial r}\right) + \frac{1}{r^2}\frac{\partial^2}{\partial \phi^2}\right) u = f(r,\phi) \quad \text{with} \quad r \in]0,1[\quad \text{and} \quad \phi \in [0, 2\pi[. \tag{1}$$

where $u(r,\phi)$ and $f(r,\phi)$ are real fields. To be quite general a Robin boundary condition is imposed at $r = 1$, viz.

$$a\, u(r=1,\phi) + b\, \left.\frac{\partial u}{\partial r}\right|_{r=1} = c(\phi) \quad \text{with} \quad \phi \in [0, 2\pi[, \tag{2}$$

where the real coefficients a and b are assumed to satisfy the ellipticity sufficient condition, $\frac{a}{b} > 0$. Dirichlet or Neumann conditions respectively correspond to fixing ($b = 0$, $a = 1$) or ($a = 0$, $b = 1$) in (2). All the fields are necessarily periodic in the azimuthal direction. They can therefore be expanded in Fourier series, with

$$\begin{pmatrix} u(r,\phi) \\ f(r,\phi) \\ c(\phi) \end{pmatrix} = \sum_{|k|=0}^{\infty} \begin{pmatrix} \bar{u}_k(r) \\ \bar{f}_k(r) \\ \bar{c}_k \end{pmatrix} e^{ik\phi} \quad , \quad \text{integer } k. \tag{3}$$

Since the left-hand-side fields are real their $k \neq 0$ Fourier components are complex conjugated, $\bar{\bullet}_k(r) = \bar{\bullet}^*_{-k}(r)$, $\bullet = u, f, c$, for $k \neq 0$. Thus, the unknown fields of the expansion (3) are those which correspond to $k \geq 0$ for example. Plugging (3) into (1) and (2) leads to the following set of mono-dimensional problems,

$$\left(\frac{1}{r}\frac{\partial}{\partial r}\left(r\frac{\partial}{\partial r}\right) - \frac{k^2}{r^2}\right)\bar{u}_k = \bar{f}_k(r) \quad \text{with} \quad r \in]0,1[\quad \text{and for} \quad k = 0, \cdots, \infty, \tag{4}$$

each completed with a boundary condition, viz.

$$a\,\bar{u}_k(r=1) + b\,\left.\frac{d\bar{u}_k}{dr}\right|_{r=1} = \bar{c}_k \quad \text{for} \quad k = 0, \cdots, \infty. \tag{5}$$

2.2. The associated homogeneous problems

The associated homogeneous problems read

$$\left(\frac{1}{r}\frac{d}{dr}\left(r\frac{d}{dr}\right) - \frac{k^2}{r^2}\right)u_k = -\lambda^2\,u_k \quad ; \quad r \in]0,1] \ , \ k = 0, \cdots, \infty, \tag{6}$$

completed with the homogeneous boundary conditions

$$a\,u_k(r=1) + b\,\left.\frac{du_k}{dr}\right|_{r=1} = 0 \quad \text{for} \quad k = 0, \cdots, \infty. \tag{7}$$

The analytical solutions to (6)-(7) express in terms of the Bessel functions of the first kind,

$$u_k(r) = J_k(\lambda\, r),$$

where λ is anyone of the roots, in infinite number, of the following equations,

$$\text{for} \quad k = 0 \ : \ a\,J_0(\lambda) = b\,\lambda\,J_1(\lambda),$$

$$\text{for} \quad k \geq 1 \ : \ a\,J_k(\lambda) + \frac{b}{2}\,\lambda\,\left(J_{k-1}(\lambda) - J_{k+1}(\lambda)\right) = 0.$$

All the λ's are real.

3. Discretized problems

3.1. The inhomogeneous problems

Let N be the radial cut-off frequency and r_p, with $p = 0, \cdots, N$, be the radial location of the Chebyshev Gauss-Radau collocation points, where

$$r_p = \frac{1}{2}\left(1 - \cos\left(\frac{(2p+1)\pi}{2N+1}\right)\right) \quad , \quad p = 0, \cdots, N. \tag{8}$$

Chosing the Gauss-Radau nodes allows us to avoid the $r = 0$ singular position which occurs in the operator (4), the closest node to $r = 0$ being at $r_0 = \frac{1}{2}\left(1 - \cos\left(\frac{\pi}{2N+1}\right)\right) \simeq \left(\frac{\pi}{2(2N+1)}\right)^2$. The discrete version of (4) and (5) is obtained by introducing the polynomial approximation of the $\bar{u}_k(r)$'s,

$$\bar{u}_k^{(N)}(r) = \sum_{p=0}^{N} \left(\bar{u}_k\right)_p \, l_p^{(N)}(r) \quad \text{with} \quad \left(\bar{u}_k\right)_p \equiv \bar{u}_k^{(N)}\left(r_p\right),$$

the $l_p^{(N)}(r)$'s being the Lagrange polynomials based over the Chebyshev Gauss-Radau nodes (8). Let $\mathbf{D}$ and $\mathbf{D}^{(2)}$ be the respective Gauss-Radau matrix representations of $\frac{d}{dr}$ and $\left(\frac{1}{r}\frac{\partial}{\partial r}\left(r\frac{\partial}{\partial r}\right)\right)$, the superscript "(2)" indicating that $\mathbf{D}^{(2)}$ is not the square of $\mathbf{D}$. The discretized version of (4) and (5) reads

$$\sum_{q=0}^{N} \mathbf{D}_{pq}^{(2)} \left(\bar{u}_k\right)_q - \frac{k^2}{r_p^2}\left(\bar{u}_k\right)_p = \left(\bar{f}_k\right)_p \quad , \quad p = 0, \cdots, N-1 \quad , \quad \text{for} \quad k = 0, \cdots, \infty, \tag{9}$$

and

$$a\,\left(\bar{u}_k\right)_N + b\sum_{q=0}^{N} \mathbf{D}_{Nq}\left(\bar{u}_k\right)_q = \bar{c}_k \quad \text{for} \quad k = 0, \cdots, \infty, \tag{10}$$

where $\left(\bar{f}_k\right)_p \equiv \bar{f}_k\left(r_p\right)$. The matrix system (9) is rectangular. It is made square upon eliminating the $\left(\bar{u}_k\right)_N$'s through (10), with

$$\left(\bar{u}_k\right)_N = \frac{\bar{c}_k - b\sum_{q=0}^{N-1} \mathbf{D}_{Nq}\left(\bar{u}_k\right)_q}{a + b\,\mathbf{D}_{NN}} \quad \text{for} \quad k = 0, \cdots, \infty.$$

The resulting discrete system reads

$$\sum_{q=0}^{N-1} \left(D_{\underline{R}}^{(2)}\right)_{pq} \left(\bar{u}_k\right)_q - \frac{k^2}{r_p^2}\left(\bar{u}_k\right)_p = \left(\bar{f}_k\right)_p - \frac{\bar{c}_k\,\mathbf{D}_{pN}^{(2)}}{a + b\,\mathbf{D}_{NN}} \;,\; p = 0, \cdots, N-1, \tag{11}$$

where

$$\left(D_{\underline{R}}^{(2)}\right)_{pq} = \mathbf{D}_{pq}^{(2)} - \frac{b\,\mathbf{D}_{pN}^{(2)}\mathbf{D}_{Nq}}{a + b\,\mathbf{D}_{NN}}. \tag{12}$$

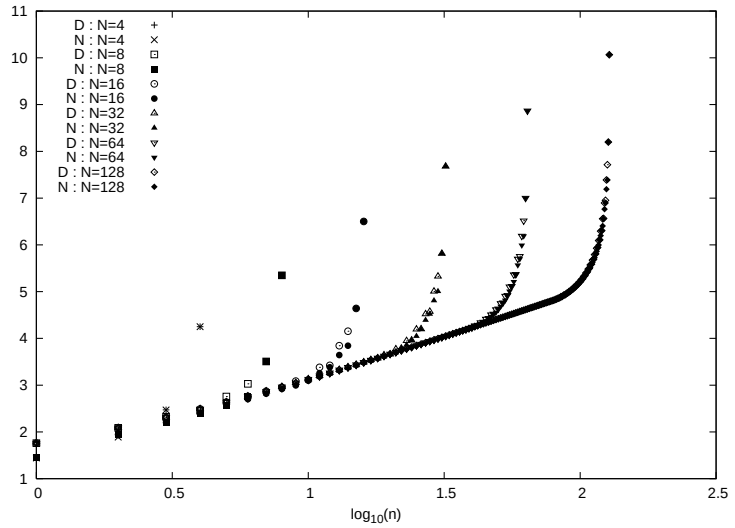

Figure 1: $\log_{10}(|\xi_n|)$ as a function of $\log_{10}(n)$, for the Dirichlet and Neumann cases, obtained with various N's and $k = 4$.

3.2. The homogeneous problems

Implementing the SDT is then based on the eigenvalues, and eigenvectors, of the matrices $\left(D^{(2)}_{\underline{R}} - \frac{k^2}{r^2}\right)$ which come from the l.h.s. of (11), wherein $\frac{k^2}{r^2}$ stands for the diagonal matrix of entries $\frac{k^2}{r_p^2}$, with $p = 0, \cdots, N-1$. Let us therefore introduce the discrete eigenvalue problem,

$$\sum_{q=0}^{N-1} \left(D^{(2)}_{\underline{R}}\right)_{pq} \left(\bar{U}_k\right)_q - \frac{k^2}{r_p^2} \left(\bar{U}_k\right)_p = \xi \left(\bar{U}_k\right)_p \ , \ p = 0, \cdots, N-1 \ \text{ for } \ k = 0, \cdots, \infty.$$

It leads to N numerical eigenvalues, ξ_n, for $n = 1, \cdots, N$, ordered with increasing absolute value of their real parts.

3.3. The numerical eigenvalues of the polar-diffusion problem

3.3.1. In the Neumann case

For the Cartesian operator, $\frac{d^2}{dx^2} + b.c.$, the numerical eigenvalues can be expressed analytically, ([4]), whereas, so far, those of $\left(D^{(2)}_{\underline{R}} - \frac{k^2}{r^2}\right)$ can only be obtained by numerical experiments. These latter were performed, for the sake of this analysis, for $N \leq 199$ and $k \leq 499$. In the Dirichlet case, viz. fixing $a = 1$ and $b = 0$ in (7) and (12), the ξ_n's were

found as being all real and negative, $\xi_n = -\lambda_n^2$ with real λ_n's, for any N and k values. The situation is fairly different in the Neumann case, $a = 0$ and $b = 1$ in (7) and (12).

Figure 1 displays the Dirichlet and Neumann numerical spectra obtained with various values of N, all with $k = 4$. The eigenvalues are all real and negative. They converge towards the analytical ones lying along the envelope which is common to all these plots. But taking now $N = 128$ and $k = 11$ for computing the Neumann spectrum leads to $(N-2)$ real negative eigenvalues, plus a pair of conjugate complex eigenvalues, while the Dirichlet ξ_n's remain all real and negative. This is shown in Fig. 2 where $\log_{10}(|Re(\xi_n)|)$ and $\log_{10}(|Im(\xi_n)|)$ are plotted as functions of $\log_{10}(n)$. Both (equal) imaginary parts are small, but definitely not compatible with the zero machine. A complete scanning of the $k(N)$ values which lead to complex eigenvalues of $\left(D_{\underline{R}}^{(2)} - \frac{k^2}{r^2}\right)$ has been made. The result is given in Fig. 3 : there is one particular value of k for each value of N, for $N \geq 13$, where complex eigenvalues occur in the Neumann spectrum.

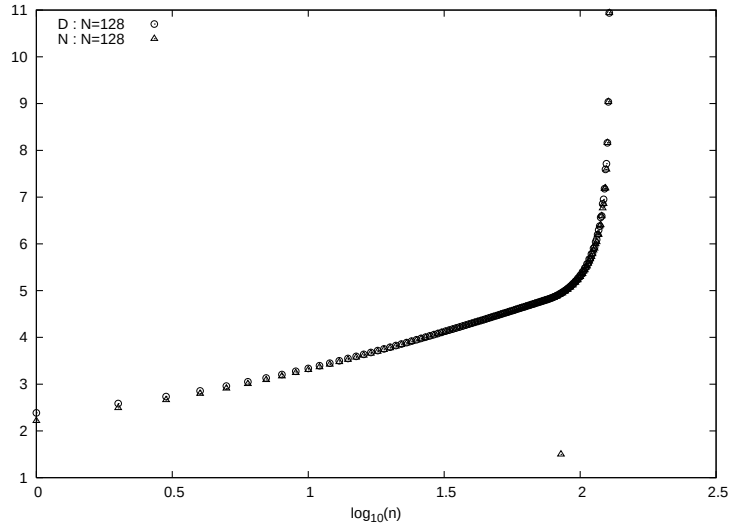

Figure 2: $\log_{10}(|Re(\xi_n)|)$ and $\log_{10}(|Im(\xi_n)|)$ as functions of $\log_{10}(n)$, for the Dirichlet and Neumann cases, obtained with $N = 128$ and $k = 11$.

Should these complex eigenvalues be considered as spurious, and/or simply due to the bad conditioning of the matrix $\left(D_{\underline{R}}^{(2)} - \frac{k^2}{r^2}\right)$? The answer is supplied by two numerical tests, both performed with $k = 39$. As indicated by Fig. 3 complex eigenvalues occur

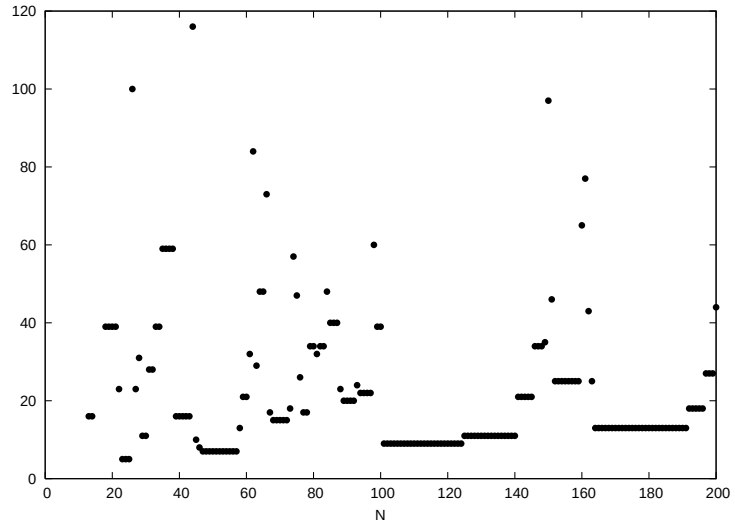

Figure 3: The set of $k(N)$ values which lead to complex eigenvalues of $\left(D^{(2)}_{\underline{R}} - \frac{k^2}{r^2}\right)$.

with $N = 19, 20, 21$ for example. First, computing them for $N = 20$ while increasing the number of significant digits, as it is made possible by the Mathematica software, shows that the complex eigenvalues are not sensitive to round-off errors. They definitely converge to more and more accurately determined values, $-11879.8 \pm 17.3509\,i$ for example. Second, computing the eigenvalues for $N = 22$, now, leads to a purely real spectrum, despite the fact that the matrix conditioning should be worst than with $N = 20$. It can thus be concluded that the complex eigenvalues are genuine eigenvalues of the discrete problem.

3.3.2. In the Robin case

When the Robin conditions (5) are adopted, and discretized using a Gauss-Radau grid with $N+1$ nodes, the order of magnitude of the Neumann contribution is $b\,N^2$. It is therefore expected that complex eigenvalues will occur in the polar-diffusion problem if $b\,N^2 \gg a$.

4. Is there a way to avoid the complex eigenvalues ?

The existence of these complex eigenvalues does not prevent from using the Successive Diagonalization Technique, but it makes it a bit more fastidious to code. Is there an easy way to suppress them ? It will be shown that a particular mapping brings a partial answer.

4.1. The mapping

In [5], D. Kosloff and H. Tal-Ezer proposed a mapping from the internal Gauss-Lobatto points to a new set of points in order to reduce, from an $\mathcal{O}(N^{-2})$ to an $\mathcal{O}(N^{-1})$ criterion, the limitation of the time step for solving the 1D hyperbolic equation. This is obtained by moving the Gauss-Lobatto nodes of abscissae y_i to other locations of abscissae x_i, according to the α-mapping relation

$$x_i = g(y_i;\alpha) = \frac{\arcsin(\alpha\, y_i)}{\arcsin(\alpha)} \in [-1,1] \quad \text{for} \quad i = 0,\cdots,N \quad \text{with} \quad 0 \le \alpha < 1.$$

For α much smaller than 1 the mapping just slightly moves the Gauss-Lobatto nodes, while values of α close to 1 lead to almost evenly distributed nodes over $[-1,1]$. We have applied this transformation on the Gauss-Radau collocation points of abscissae $0 < r_i \le 1$, with $i = 0,\cdots,N$, for solving the radial diffusion equation (11). Any function $f(r)$ is then transformed into $h(x)$ whose first derivative is obtained from

$$\frac{dh}{dx} = \frac{1}{g'(r;\alpha)}\frac{df}{dr} \quad \text{with} \quad g'(r;\alpha) = \frac{\partial g}{\partial r}.$$

The radial discrete first derivative $\mathbf{D}$ is transformed as

$$\mathbf{D} \rightarrow \mathbf{A}\cdot\mathbf{D}$$

where $\mathbf{A}$ is a diagonal matrix whose entries are given by

$$\mathbf{A}_{ii} = \frac{1}{g\prime(r_i;\alpha)} = \frac{\alpha}{\arcsin(\alpha)\sqrt{1-(\alpha\, r_i)^2}} \quad , \quad i = 0,\cdots,N.$$

In the same way, the matrix $\mathbf{D^2}$ which represents $\frac{d^2}{dr^2}$ is modified according to

$$\mathbf{D^2} \rightarrow \mathbf{A}^2\cdot\mathbf{D^2} + \mathbf{B}\cdot\mathbf{D},$$

the diagonal matrix $\mathbf{B}$ being defined by

$$\mathbf{B}_{ii} = -\frac{g\prime\prime(r_i;\alpha)}{[g\prime(r_i;\alpha)]^3} \quad , \quad i = 0,\cdots,N,$$

where

$$g\prime\prime(r_i;\alpha) = \frac{\alpha^3}{\arcsin(\alpha)}\cdot\frac{r_i}{[1-(\alpha\, r_i)^2]^{3/2}}.$$

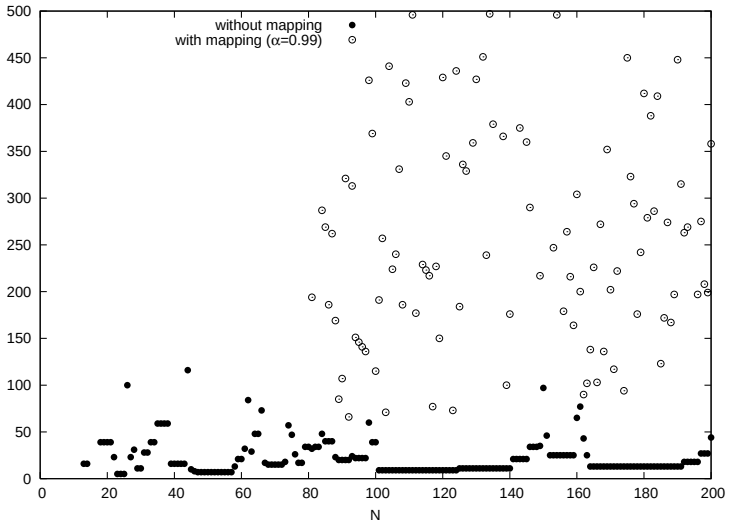

Figure 4: The set of $k(N)$ values leading to complex eigenvalues of $\left(D^{(2)}_{\underline{R}} - \frac{k^2}{r^2}\right)$, with ($\alpha = 0.99$) and without mapping.

4.2. Its impact on the polar-diffusion spectrum

Figure 4 shows the way the $k(N)$ configuration which leads to complex eigenvalue has been modified with the $\alpha = 0.99$ mapping. Complex eigenvalues are still occurring, but for higher values of N, viz. $N > 80$, and also for much larger values of k.

Thus, thanks to the mapping, spectra which were previously "polluted" by complex eigenvalues are now purely real. But does this mapping affect, and to what extent, the spectrum itself of the polar-diffusion operator ? Let us denote $\xi^{(\alpha)}$ the set of the numerical eigenvalues obtained from an α-mapping and compare them to those, ξ, obtained without mapping. One of the Neumann cases presented in Fig. 1 is chosen, the one which corresponds to $N = 128$, $k = 4$. In Fig. 5 are plotted the relative differences $\left|\frac{\xi_n^{(\alpha)} - \xi_n}{\xi_n}\right|$ obtained for several values of α. Two regions clearly show up. The first region is the part of the spectra where the numerical eigenvalues are in good agreement with the analytical ones, the common envelope in Fig. 1. The mapping significantly affects the accuracy of the numerical eigenvalues, but at a level which is without any practical importance. The second region lies in the purely numerical part of Fig. 1, wherein the eigenvalues strongly depart from the analytical ones. This is the region of Fig. 5 which exhibits a very steep increasing of the

relative differences. Are there practical consequences of this behavior ? The largest absolute value of the numerical eigenvalues obtained with the Gauss-Radau grid is expected to scale, asymptotically with N, as $\mathcal{O}(N^4)$. This is what makes the (Chebyshev) spectral method able of efficiently capturing the boundary layers close the solid boundaries of the flow. Figure 6 shows that this scaling drifts, as expected, to an asymptotic law $\mathcal{O}(N^2)$ when the mapping is performed with α extremely close to 1. Discrepancies are therefore expected, in boundary layer regions, between numerical flows obtained with and without this mapping.

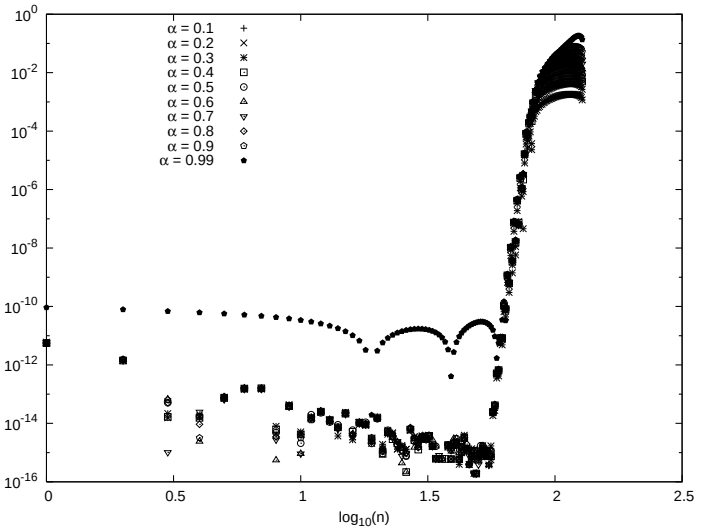

Figure 5: Relative differences $\left|\frac{\xi_n^{(\alpha)}-\xi_n}{\xi_n}\right|$, for the Neumann cases, obtained with various N's and $k=4$ with several values of α.

4.3. Mapping and accuracy

Choosing the Gauss-Radau (or Gauss-Lobatto) nodes for discretizing the differential equations is not made by convenience. It is indeed well known ([6]) that using these nodes is at the heart of the high level of numerical accuracy the spectral methods are able to achieve. It is therefore expected that the mapping should degrade the overall accuracy of the Gauss-Radau scheme, more and more with increasing α.

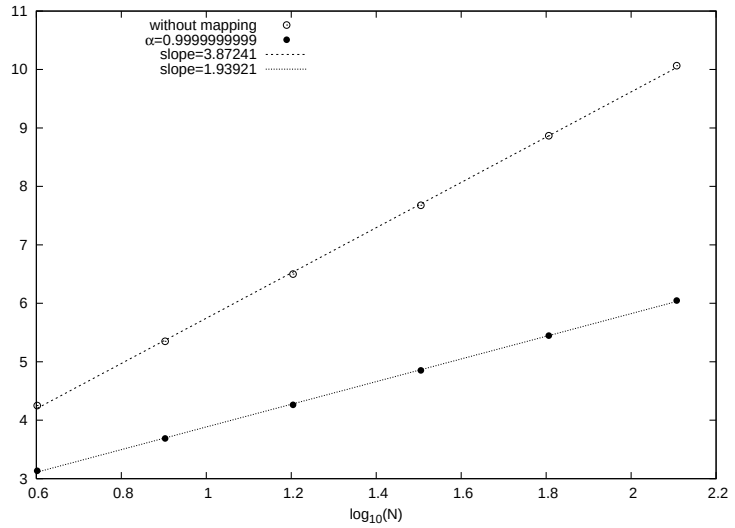

Figure 6: Scaling laws in $\mathcal{O}\left(N^{\beta}\right)$ of the largest $|\xi_n|$ and $|\xi_n^{(\alpha)}|$, for the Neumann cases, obtained with $\alpha = 0.9999999999$. They suggest the asymptotic laws $max_n|\xi_n| \simeq \mathcal{O}\left(N^4\right)$ and $max_n|\xi_n^{(\alpha)}| \simeq \mathcal{O}\left(N^2\right)$.

4.3.1. Comparison with an analytical solution of the polar-diffusion problem

Consider the equation

$$\left(\frac{1}{r}\frac{\partial}{\partial r}\left(r\frac{\partial}{\partial r}\right) - \frac{k^2}{r^2}\right) u = f(r) \quad , \quad r \in]0,1[, \tag{13}$$

where the source term is chosen as being $f(r) = (N^2 - k^2)\, r^N$. The analytical solution is a polynomial, $u(r) = r^N$, which will coincide (within the zero machine accuracy) with the numerical solution provided by the Gauss-Radau Chebyshev solver of (13). This solution of (13) can be considered with the Neumann boundary condition $\frac{du}{dr}\big|_{r=1} = N$. It is then very easy with this analytical solution to compute the error coming from the α-mapping solver, wheresoever are located the associated nodes. Let $u^{(N)}(r_p)$, for $p = 0, \cdots, N$, be the nodal values obtained from this latter solver, and $E = max_{p=0,\cdots,N-1}\left|\frac{u^{(N)}(r_p) - r_p^N}{r_p^N}\right|$ be the relative error in absolute norm between the analytical and numerical solutions. Figure 7 shows the error E as a function of the mapping parameter α for various N values. For small α values or large N the error is very small.

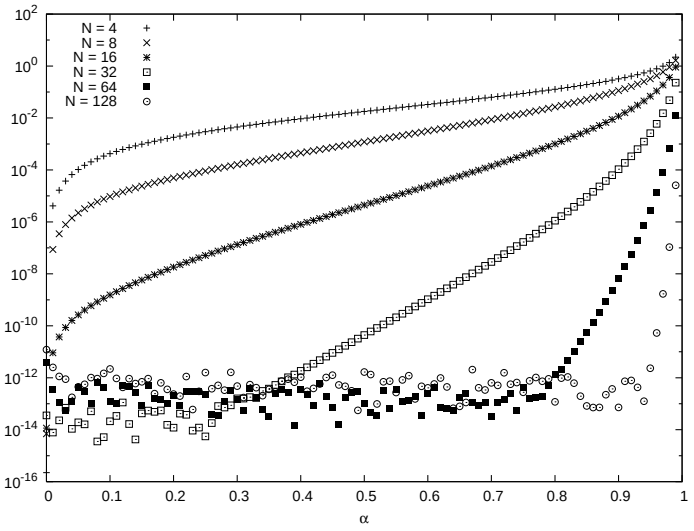

Figure 7: Maximum relative error E for different N as functions of α, for $k = 4$.

4.3.2. Comparison on a physical configuration

We now consider the axi-symmetric floating-zone problem in microgravity environment which is described in detail in [7] and [8]. A cylindrical liquid bridge, of height $2H$ and radius R, is maintained by surface tension between two horizontal isothermal solid disks. Its lateral free surface is submitted to a steady and uniform heat flux. This triggers and maintains a thermo-capillary flow : the surface tension variations, due to the thermal gradients on the free surface, generate tangential stresses and then viscous driving of the liquid. The flow is generally studied in a two-parameter space : the Prandtl number (Pr), ratio between momentum and thermal diffusivities, and the Marangoni number (Ma), ratio between thermocapillary and thermal diffusion velocities. The axi-symmetric velocity and temperature fields of the flow were deeply studied on a large domain of the parameters space in [7] and [8]. The impact of the numerical treatment of the vorticity singularity which occurs at the junction of the free surface with the rigid disks was explored in [9] and [10].

The axi-symmetric physical problem is governed by the following non-dimensional Navier-

Stokes and energy equations, in the Boussinesq approximation framework,

$$\frac{\partial \boldsymbol{u}}{\partial t} + (\boldsymbol{u}.\boldsymbol{\nabla})\,\boldsymbol{u} = -\boldsymbol{\nabla} p + Pr\,\left(\boldsymbol{\nabla}^2 - \frac{\boldsymbol{e}_r}{r^2}\right)\boldsymbol{u}, \tag{14}$$

$$\frac{\partial \theta}{\partial t} + (\boldsymbol{u}.\boldsymbol{\nabla})\,\theta = \boldsymbol{\nabla}^2\theta, \tag{15}$$

$$\boldsymbol{\nabla}.\boldsymbol{u} = 0, \tag{16}$$

where $\boldsymbol{u}$, θ and p respectively are the non-dimensionnal velocity, temperature and pressure. The unit vectors $\boldsymbol{e}_r$ and $\boldsymbol{e}_z$ define respectively the radial and axial directions, their origin being located at the center of the liquid bridge. The operators are defined as follows: $\boldsymbol{\nabla} = \boldsymbol{e}_r\,(\partial/\partial r) + \boldsymbol{e}_z\,(\partial/\partial z)$, $\boldsymbol{\nabla}^2 = (1/r)(\partial/\partial r)[(r(\partial/\partial r))] + \partial^2/\partial z^2$. Noting $\boldsymbol{u} = v\,\boldsymbol{e}_r + w\,\boldsymbol{e}_z$, one has also $\boldsymbol{\nabla}.\boldsymbol{u} = (1/r)[\partial(rv)/\partial r] + (\partial w/\partial z)$ and $\boldsymbol{u}.\boldsymbol{\nabla} = v(\partial/\partial r) + w(\partial/\partial z)$.

To complete the set (14)-(16), boundary conditions are specified:

$$\bullet\ z = \pm 1 \quad \begin{cases} \boldsymbol{u} = \boldsymbol{0}\ \text{(no-slip conditions)}, \\ \theta = 0\ \text{(imposed temperature)}, \end{cases}$$

$$\bullet\ r = 1 \quad \begin{cases} v = 0\ \text{(non-deformable free surface)}, \\ \dfrac{\partial w}{\partial r} = -Ma\,\dfrac{\partial \theta}{\partial z} f(z)\ \text{(stress condition)}, \\ \dfrac{\partial \theta}{\partial r} = q(z)\ \text{(heat flux)}. \end{cases} \tag{17}$$

with $q(z) = (1 - z^2)^2$ the heat flux. The parameter values are $Pr = 0.01$ and $Ma = 106$. The function $f(z) = (1 - z^{2n})^2$ is introduced for regularizing the vorticity singularity, n being here fixed to 13 according to the results of [9] and [10].

The system (14) - (17) is space-discretized with a Chebyshev collocation method based on radial Gauss-Radau and axial Gauss-Lobatto grids. Uncoupling the velocity and pressure fields is made with the Projection-Diffusion method, ([11]). The time integration is performed with an usual second order finite difference scheme. Let w_{ij} be the set of the axial velocity nodal values obtained in this way, and w_{ij}^{map} the corresponding set obtained from a mapping applied on the radial grid, the α parameter being fixed to 0.99.

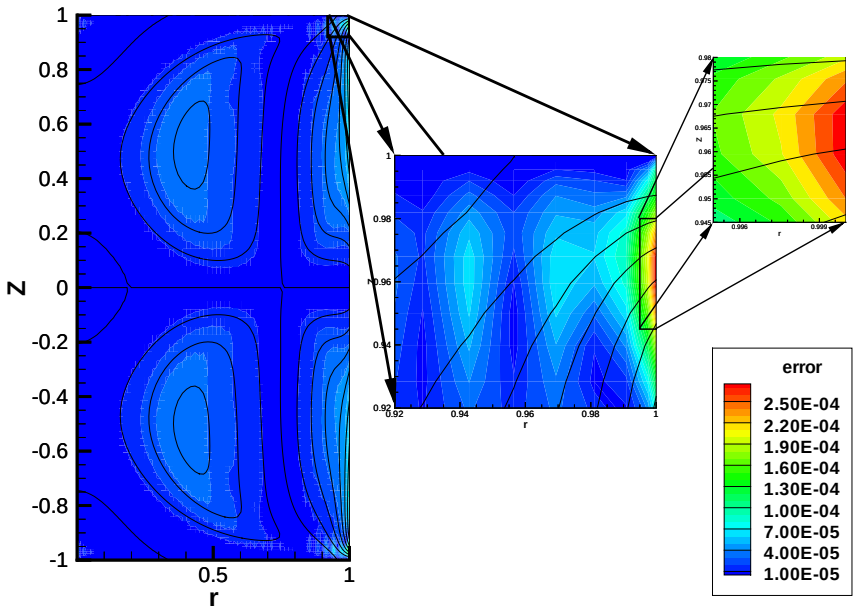

Figure 8: Maximum relative error E on the axial velocity field w and iso-w lines for $Ma = 106$ and $Pr = 0.01$.

Figure 8 shows the relative error

$$E = \frac{\max_{i,j} |w_{ij}^{map} - w_{ij}|}{\max_{i,j} |w_{ij}^{map}|} \tag{18}$$

obtained with 70 and 100 grid points in the radial and axial directions respectively. In this figure are superimposed the iso-w lines supplied by the mapped ($\alpha = 0.99$) Gauss-Radau grid. As expected from the comment made from Fig. 5 the maximum of the error is located in the regions of steep vorticity gradient. Yet this relative error is small. The grid transformation can thus be used in order to avoid complex conjugate eigenmodes.

5. Conclusion

The Chebychev Gauss-Radau discrete version of the polar-diffusion operator, $L = \left(\frac{1}{r}\frac{\partial}{\partial r}\left(r\frac{\partial}{\partial r}\right) - \frac{k^2}{r^2}\right)$, associated with a Neumann boundary condition at $r = 1$, does not preserve the ellipticity which is expected for L in the continuous realm. Numerical complex conjugate eigenvalues are indeed obtained for a set of values of both the azimuthal wave-number k and the

Gauss-Radau cut-off frequency. We have shown that these complex eigenvalues are genuine eigenvalues of the discrete version of L. It is proposed in this paper to avoid them through a transformation of the Gauss-Radau grid. Although this mapping affects significantly the L eigenvalues of largest absolute value, its impact on the solution numerical accuracy, measured on an analytical test, is very small, in case of moderate shifts of the Gauss-Radau points. The evaluation of the error, in a physical problem presenting steep vorticity gradients, shows that the grid transformation can be used to avoid the complex conjugate eigenvalues.

[1] P. Haldenwang, G. Labrosse, S. Abboudi, M. Deville, Chebyshev 3D Spectral and 2D Pseudospectral Solvers for the Helmholtz Equation, J. Comput. Phys. 55 (1984) 115–128.

[2] R. Lynch, J. Rich, D. Thomas, Direct Solution of Partial Differential Equations by Tensor Product Methods, Numer. Math. 6 (1964) 185–199.

[3] S. Nguyen, C. Delcarte, A spectral collocation method to solve Helmoltz problems with boundary conditions involving mixed tangential and normal derivatives, J. Comput. Phys. 200 (2004) 34–49.

[4] H. Vandeven, On the eigenvalues of second-order spectral differentiation operators, Comput. Methods Appl. Mech. Engrg. 80 (1990) 313–318.

[5] D. Kosloff, H. Tal-Ezer, A modified Chebyshev pseudospectral method with an $O(N^{-1})$ time step restriction, J. Comput. Phys. 104 (1993) 457–469.

[6] C. Canuto, M. Hussaini, A. Quarteroni, T. Zang, Spectral Methods in Fluid Dynamics, Springer Series in Computational Physics, Springer-Verlag, New York, 1988.

[7] E. Chénier, C. Delcarte, G. Labrosse, Stability of the axisymmetric buoyant-capillary flows in a laterally heated liquid bridge, Phys. Fluids 11(3) (1999) 527–541.

[8] E. Chénier, C. Delcarte, G. Kasperski, G. Labrosse, Sensitivity of the liquid bridge hydrodynamics to local capillary contributions, Phys. Fluids 14(9) (2002) 3109–3117.

[9] G. Kasperski, G. Labrosse, On the numerical treatment of viscous singularity in wall-confined thermo-capillary convection, Phys. Fluids 12(11) (2000) 2695–2697.

[10] E. Chénier, C. Delcarte, G. Kasperski, G. Labrosse, Thermocapillary flows and vorticity singularity, Interfacial Fluid Dynamics and Transport Process, Lecture Notes in Physics, vol. 628, R. Narayanan and D. Schwabe Eds., Springer-Verlag, Berlin, Heidelberg, New York, 2003.

[11] E. Leriche, G. Labrosse, High-order direct Stokes solvers with or without temporal splitting : numerical investigations of their comparative properties, SIAM J. Scient. Comput. 22(4) (2000) 1386–1410.